Wind-Driven Sea Level Variability on the California Coast: An Adjoint Sensitivity Analysis

ARIANE VERDY, MATTHEW R. MAZLOFF, AND BRUCE D. CORNUELLE

Scripps Institution of Oceanography, University of California, San Diego, La Jolla, California

SUNG YONG KIM

Division of Ocean Systems Engineering, School of Mechanical, Aerospace and Systems Engineering, Korea Advanced Institute of Science and Technology, Daejeon, South Korea

ABSTRACT

Effects of atmospheric forcing on coastal sea surface height near Port San Luis, central California, are investigated using a regional state estimate and its adjoint. The physical pathways for the propagation of nonlocal [$O(100\,\mathrm{km})$] wind stress effects are identified through adjoint sensitivity analyses, with a cost function that is localized in space so that the adjoint shows details of the propagation of sensitivities. Transfer functions between wind stress and SSH response are calculated and compared to previous work. It is found that (i) the response to local alongshore wind stress dominates on short time scales of $O(1\,\mathrm{day})$; (ii) the effect of nonlocal winds dominates on longer time scales and is carried by coastally trapped waves, as well as inertia–gravity waves for offshore wind stress; and (iii) there are significant seasonal variations in the sensitivity of SSH to wind stress due to changes in stratification. In a more stratified ocean, the damping of sensitivities to local and offshore winds is reduced, allowing for a larger and longer-lasting SSH response to wind stress.

1. Introduction

Sea level variations impact coastal communities, making them a subject of great societal importance. Climate change induces long-term trends in global and regional sea level (e.g., Nicholls and Cazenave 2010; Kemp et al. 2011). Meanwhile, air–sea fluxes of buoyancy and momentum account for much of the nontidal variability on shorter time scales, ranging from hours to months. Understanding the ocean sensitivity to atmospheric forcing is useful for illuminating local dynamics and thus predicting the regional ocean response to weather events and climate variability. This study highlights the physical pathways that force high-frequency variability of coastal sea surface height (SSH) in a state estimate of the California Current System.

The California Current System is a region of high biological productivity sustained by wind-driven coastal upwelling (Huyer 1983), which brings nutrient-rich deep waters to the sunlit surface layers. Seasonal and interannual variability in upwelling due to shifting wind patterns influences plankton and fish populations of the California Current Ecosystem (Rykaczewski and Checkley 2008; Chenillat et al. 2013). Understanding the variability in coastal SSH, which is intrinsically linked to coastal upwelling, may bring new insight on the processes leading to observed fluctuations in nutrient supply and biological productivity. Surface wind stress and buoyancy fluxes also influence the local ecosystem by setting up the stratification and horizontal circulations (Checkley and Barth 2009). As surface geostrophic transport is determined by the difference between near- and offshore SSH, understanding the sensitivity of coastal SSH is a first step in understanding what controls the transport of the California Current and undercurrent.

While local winds affect coastal SSH through Ekman transport and pumping, coastally trapped waves can carry the effect of nonlocal winds (Brink 1991). In the California Current System, coastally trapped waves are found to propagate sea level anomalies over hundreds of kilometers (Battisti and Hickey 1984; Chapman 1987; Pringle and Riser 2003). Using a numerical simulation,

Corresponding author address: Ariane Verdy, Scripps Institution of Oceanography, 9500 Gilman Dr., La Jolla, CA 92093.
E-mail: averdy@ucsd.edu

Pringle and Dever (2009) showed that coastal currents in the Southern California Bight are influenced by remote winds both within and outside the California coast region. Ryan and Noble (2006) examined the relation between sea level on the California coast and alongshore winds through a regression analysis between tide gauge and wind buoy data, including local (within ~100 km) and remote [$O(1000 \, \text{km})$] winds. They found that non-local winds contribute significantly, their effect lasting more than 3 months at some stations. They also considered responses at longer periods, including ENSO, but did not exclude ENSO effects on sea level that are unrelated to winds.

An adjoint model separately evaluates the sensitivity to each forcing mechanism, thus avoiding statistical noise and correlations between forcing mechanisms that can affect regression analyses. Veneziani et al. (2009) used an adjoint model to analyze the sensitivity of several aspects of the California Current System, including coastal SSH. Consistent with the aforementioned studies, they find that coastal SSH is sensitive to both local and remote forcing, that the sensitivity persists for at least the 2-week duration of their adjoint run, and that the sensitivity depends on the forward model ocean state. Identifying and quantifying the mechanisms and pathways of sensitivity propagation remains, however, an open question, as is the propagation of sensitivity southward past Point Conception.

This work uses the adjoint of an ocean general circulation model to diagnose the response of SSH near Port San Luis, off the coast of central California, to atmospheric forcing. Linearized physical pathways propagating the effects of surface wind stress, heat fluxes, and freshwater fluxes are identified through the adjoint sensitivity analyses. The goal is to analyze the evolution of the sensitivity over the model domain for times ranging from hours to months, thus addressing the question of what forces SSH variability in both time and space.

Our analysis extends the work of Veneziani et al. (2009), who performed a 14-day adjoint model run to compute the sensitivity of squared SSH over the 14-day period and over an approximately 50-km strip adjacent to the coast between 35° and 40°N. In contrast, by using higher viscosity to damp small-scale structures, which tend to be nonlinear, the experiments presented here use a 100-day adjoint model run and compute the sensitivity of SSH (i.e., a linear objective function) at a single point in space and time. The lack of averaging in the objective function makes it easier to follow the back propagation of different wave types and modes from a single target point.

The adjoint-derived sensitivities are SSH response functions that can be Fourier transformed into transfer functions for comparison with those estimated from observations by Ryan and Noble (2006). We examine both the response (section 4a) and the transfer function (section 4c) with respect to momentum input from the wind, the main driver of SSH variability. The SSH response to local and remote winds clearly shows the barotropic storm surge response during the first few hours as well as the slower propagation of coastally trapped waves and inertia–gravity waves. Integrations in summer and winter reveal differences between the wind-driven responses due to the influence of seasonally varying stratification (as discussed in section 5).

Because the adjoint model solves a set of equations that are linearized around the background ocean state, adjoint-derived sensitivities are a linear approximation to the nonlinear SSH response. Linear analysis provides an insight into the physics, and is commonly employed to compute transfer functions (e.g., Ryan and Noble 2006) and wave propagation (e.g., Pringle and Riser 2003). Nonlinear effects may be significant, especially at shorter length scales, and adjoint model results should be interpreted cautiously (Powell et al. 2008; Moore et al. 2009; Zhang et al. 2011, 2012). However, for the problem of interest, the linearity assumption is shown to hold well for the 100-day period of integration. This is demonstrated by the nonlinearity check in perturbation experiments (section 3); the high skill from the hindcast experiment, which is linear in nature (section 4b); and the success of the multiyear state estimation process, which employs adjoint-derived sensitivities to minimize the model–observations misfit (as briefly described in section 2).

2. Methods: An adjoint model for state estimation and sensitivity analysis

A state estimate of the California Current System has been produced for the period from 1 January 2007 to 31 July 2009 using the machinery developed by the Estimating the Circulation & Climate of the Ocean (ECCO) consortium (Wunsch and Heimbach 2007). This involves optimizing inputs to the Massachusetts Institute of Technology (MIT) General Circulation Model [MITgcm; evolved from Marshall et al. (1997)] to bring the model solution into consistency with observations. Optimization is accomplished iteratively via the adjoint method [described, e.g., in Stammer et al. (2003) or Wunsch (2006)], using observations available for the time window of the simulation to adjust "controls" consisting of atmospheric state, open boundary conditions, and initial conditions for the model. The state estimate is a free-forward simulation using the optimized controls. The long-term assimilation window (942 days) means that the observations are combined in a continuous, dynamically consistent hindcast (without unphysical nudging terms).
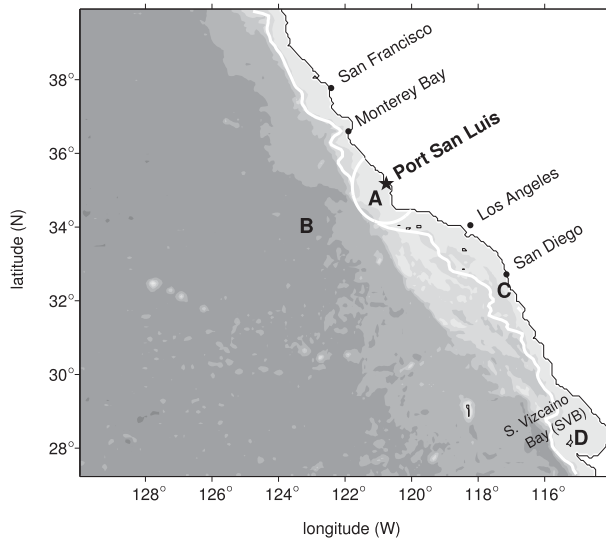
FIG. 1. Model domain. Shaded contours show the bathymetry with a 1000-m interval. White contours split the domain into three regions: the "local" area within 1° of Port San Luis tide gauge (Port San Luis), the "coastal" area with a depth <1500 m, and the "offshore" area. Letters mark specific locations of interest for the analysis.

TABLE 1. Parameter values used for forward (FWD) and adjoint (ADJ) model runs.

Parameter	Units	Value
Vertical viscosity	$m^2 s^{-1}$	1×10^{-4}
Horizontal viscosity (FWD)	$m^2 s^{-1}$	1×10^2
Horizontal viscosity (ADJ)	$m^2 s^{-1}$	1×10^3
Biharmonic horizontal viscosity	$m^4 s^{-1}$	1×10^9
Quadratic bottom drag	Dimensionless	1×10^{-3}
Vertical diffusivity	$m^2 s^{-1}$	1×10^{-5}
Horizontal diffusivity	$m^2 s^{-2}$	1×10^0

The model domain, shown in Fig. 1, extends from 27.2° to 40°N and from 130°W up to the coast. It encompasses most of the California coastline and ends just south of Punta Eugenia in Baja California. The model has a ¹/₁₆° horizontal resolution and 72 vertical levels of variable thickness. The bathymetry and coastline are derived from 2-Minute Gridded Global Relief Data (ETOPO2v2; http://www.ngdc.noaa.gov/mgg/fliers/06mgg01.html). The governing equations are stepped forward with a 20-min time step. The model is forced through an atmospheric boundary layer scheme where fluxes of heat, freshwater (salt), and momentum are determined by bulk formulas (Large and Pond 1981). The 6-hourly atmospheric forcing from the National Centers for Environmental Prediction–North American Mesoscale Forecast System (NCEP–NAM; http://www.emc.ncep.noaa.gov/NAM) is applied. Although this forcing is optimized using the adjoint method, the wind product is altered by less than 20%, and is hereafter referred to as NAM winds. Initial conditions and boundary conditions for the north, west, and south open boundaries are optimized, with first-guess fields derived from a global 1°-resolution state estimate (Forget 2010). Tidal forcing is not included. River runoff, estimated from Fekete et al. (2002), is prescribed at the coast. The model employs the nonlocal K-profile parameterization (KPP) for vertical mixing (Large et al. 1994). Values of viscosity, bottom drag, and diffusivities used are given in Table 1. It has been shown that for these given parameter values and this model resolution,

mesoscale structure greater than 30 km is resolved, while submesoscale variance is underestimated (Todd et al. 2012). In the western California Current System, the SSH wavenumber spectrum is red (Kim 2010; Kim et al. 2011; Sasaki and Klein 2012), thus there is relatively less energy associated with submesoscale physics for the particular problem investigated here.

The model and solution have been previously described in Todd et al. (2011, 2012), who analyzed the 64th iteration of the assimilation. These studies found the state estimate to capture the structure and temporal variability of ocean currents on scales larger than about 30 km, although simulated current speeds tended to be smaller than observed. The present study uses the 108th iteration (described in section 2a), which is largely consistent with observations. Having a realistic forward model state and dynamics gives confidence that the response of the state estimate is representative of processes in the real ocean, and that it is useful for analyzing the response of SSH to wind perturbations.

a. Estimated ocean state

The state estimate is analyzed primarily in the central California coast area, around Port San Luis. This region is sufficiently far from the model's open boundaries, which can sometimes introduce artifacts in the solution. The Port San Luis tide gauge, located at 35.18°N, 120.76°W, provides a continuous record of SSH during the time period considered. The simulated time series of SSH variations near the coast at 35.1°N (close to the actual location of Port San Luis) is compared to the tide gauge data. As can be seen in Fig. 2, the state estimate captures the amplitude of observed interannual variability, but not the timing, leading to a poor correlation of the two time series. At a low frequency, the power spectrum of SSH from the state estimate is similar to that of the observations (Fig. 2b); however, the model energy is low at higher frequencies, in the same way that the power spectrum of the local NAM winds is also low compared to wind buoy data (Fig. 2c). Farther offshore, the simulation is in good agreement with
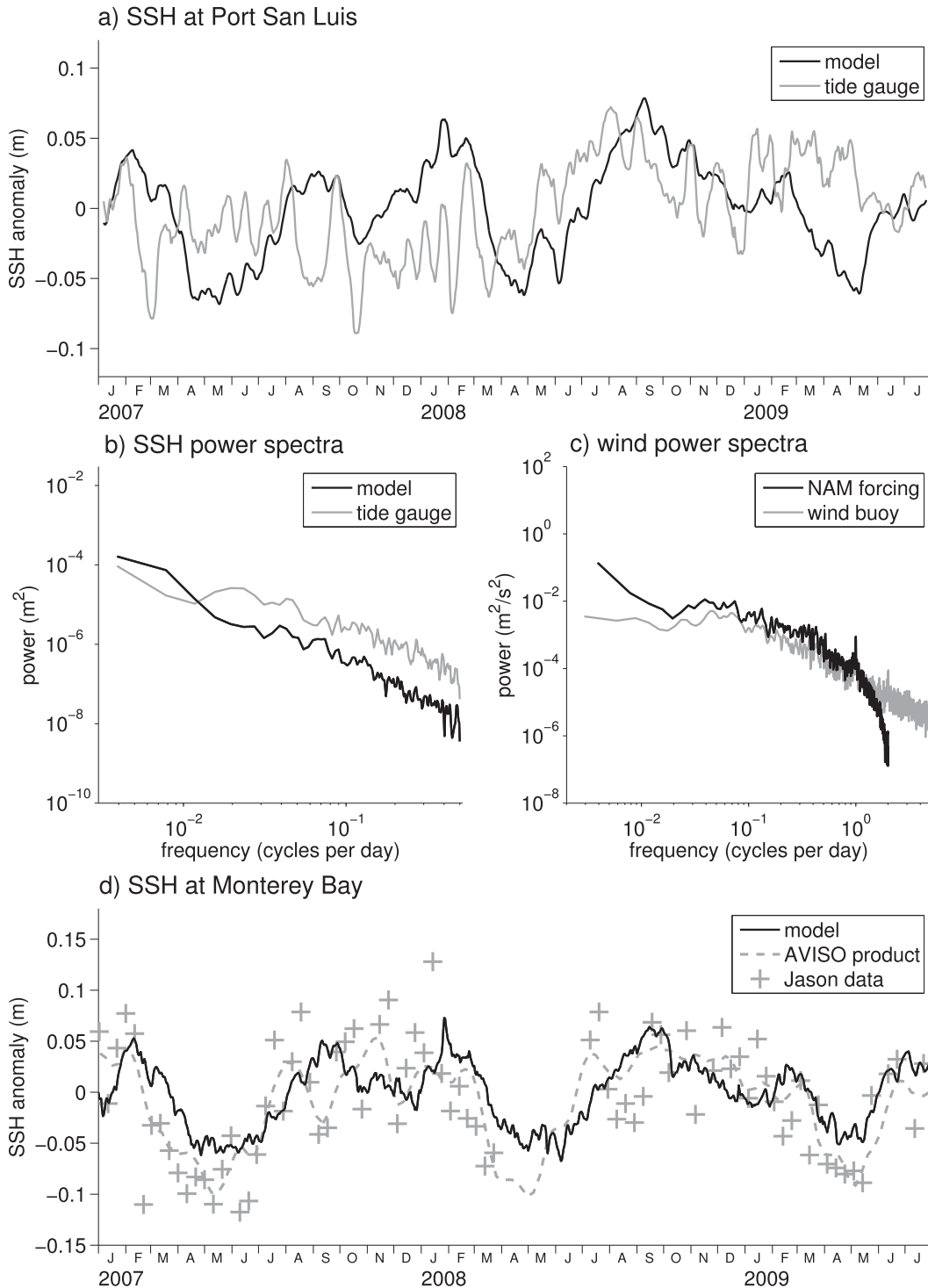
FIG. 2. (a) Time series of SSH anomalies at Port San Luis: observed (gray) and modeled (black), smoothed with a 10-day running mean. (b) Power spectral density of observed and modeled SSH anomalies at Port San Luis, estimated via Welch's method [data from the National Oceanographic and Atmospheric Administration (NOAA) Center for Operational Oceanographic Products and Services; http://tidesandcurrents.noaa.gov/]. (c) Power spectral density of meridional wind anomalies at the Santa Maria buoy, observed (gray; from National Data Buoy Center; http://www.ndbc.noaa.gov/) and NAM (black) winds. (d) Time series of SSH anomalies near Monterey Bay (36.5°N, 122.3°W): AVISO (dotted gray curve), Jason (crosses), and modeled (black curve).
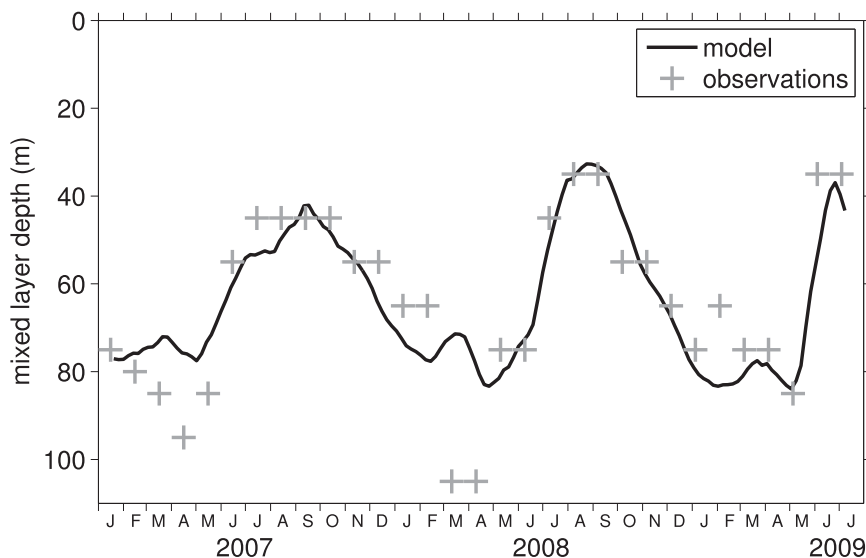
FIG. 3. MLD in a $1° \times 1°$ box near Port San Luis. Running mean (30 day) of the simulated (solid curve) and monthly-averaged MLD calculated from observed temperature and salinity from Spray gliders (gray crosses; from Todd et al. 2012).

altimetric data. In Fig. 2d, the simulated SSH near Monterey Bay (36.5°N, 122.3°W) is compared to the optimally interpolated Archiving, Validation, and Interpretation of Satellite Oceanographic data (AVISO) product (http://www.aviso.oceanobs.com/). The model is constrained to along-track altimetric observations, among other data sources, but not to this gridded AVISO product. A Jason altimetry line falls close to that location, which is coastal but off of the shelf (the local ocean depth is 1300 m).

Stratification, which strongly influences the effect of winds on SSH (see sections 4a and 4c), is consistent with observations (e.g., the Spray gliders; Todd et al. 2011). Observed and simulated mixed layer depths (MLD) around Port San Luis are shown in Fig. 3. MLD is calculated, following de Boyer Montégut et al. (2004), as the depth where density exceeds the surface density by $\Delta\rho = 0.5 \text{ kg m}^{-3}$ (other density thresholds give qualitatively similar results). The MLD near Port San Luis exhibits a strong seasonal cycle and there is good agreement with MLD calculated from densities inferred from glider data, with the exception of the amplitude of the deep mixed layers observed during the winters of 2007 and 2008.

Discrepancies between the California Current System state estimate SSH and the tide-gauge observations at Port San Luis (Fig. 2a) likely involve strong small-scale gradients not resolved in the model and, to some extent, the model not resolving finescale bathymetry and coastal structure. Comparing a single model grid point with a single tide gauge is a hard test for any model. At wider

spatial scales, the state estimate agrees well with the observations, capturing the forward model ocean state and its statistics while obeying the physics as represented by an ocean general circulation model.

b. Adjoint sensitivities

The same adjoint model used for optimization of the state estimate can be employed to perform a sensitivity analysis. The adjoint model calculates the partial derivatives of all state variables around a time-dependent "forward" model trajectory. Adjoint sensitivities show where and when perturbations in the model forcing would lead to a specific response. (In contrast, a forward perturbation experiment shows where and when the system responds to a specific perturbation.) Here the response considered is the change in SSH at Port San Luis. In essence, we perturb the SSH and iterate the ocean physics backward to determine what model inputs are capable of making such a change. To determine the sensitivity of SSH to an earlier model state using the forward model would require many simulations with a suite of model input perturbations, and thus be computationally prohibitive. The adjoint method has been widely used to quantify the relative importance of different forcing mechanisms, whether it be the type or scale of forcing; recent examples include Moore et al. (2009), Veneziani et al. (2009), Zhang et al. (2011), Tulloch et al. (2011), and Todd et al. (2012). Losch and Heimbach (2007) provide additional information on the use of adjoint models to probe the sensitivity of ocean general circulation models. The equivalence between adjoint and

regression analyses is explained in Zhang et al. (2011). A brief description is given below for readers who may not be familiar with the adjoint method.

The adjoint effectively computes the Green's function for the response at a specific time and location to perturbations anywhere in the domain. The Green's function g relating the response y to the driving force f as a function of space and time is

$$y(\mathbf{x}, t) = \int_{\mathbf{x}'} \int_{t'} g(\mathbf{x}, t, \mathbf{x}', t') f(\mathbf{x}', t') \, dt' \, d\mathbf{x}', \qquad (1)$$

where $(\mathbf{x}, t)$ is the space and time location of the response and $(\mathbf{x}', t')$ is the space and time location of the forcing. The relation is much simpler if g depends only on $\mathbf{x} - \mathbf{x}'$ and $t - t'$, such that the integral becomes a convolution, and the number of unknowns in g is greatly reduced. In either case, Eq. (1) can be written in operator form as

$$\mathbf{y} = G\mathbf{f}, \qquad (2)$$

where the space and time dimensions of y and f have been represented as a vector and the kernel g is represented as an operator, so the integral is expressed as a product of the operator G with f. In complicated systems like the ocean case here, g is a function of eight dimensions, and cannot be fully estimated. Forward perturbation experiments can address a single $f(\mathbf{x}', t')$ at a time, while adjoint experiments can address a single $y(\mathbf{x}, t)$ at a time. In this case, we focus on the response at a single point, so only one adjoint run is needed, although the response can vary with ocean state and so must be repeated at different times to assess seasonal effects.

A scalar objective function $J = J(y)$ can be defined such that the adjoint model solves for the sensitivity

$$\frac{\partial J}{\partial \mathbf{f}(\mathbf{x}', t')}, \qquad (3)$$

where $\mathbf{f}$ represents all model variables and inputs (Giering and Kaminski 1998), thus determining the sensitivity of J to independent components of the model solution. In this work the objective function is defined as

$$J \equiv \eta(\mathbf{x}, t), \qquad (4)$$

where η is SSH.

Objective functions J can be arbitrarily complex functions of the response y. Quadratic functions are a common choice, mainly because of the similarity to the least squares objective function used in adjoint optimization.

For example, Veneziani et al. (2009) considered the function $J = \eta^2$, integrated along the coastline and over a 2-week period. For a quadratic objective function, the sensitivity is given by $\partial J/\partial f = 2\eta(\partial \eta/\partial f)$. The factor 2η becomes a weighting function that is determined by the forward model state. This is problematic for interpreting the sensitivity, especially for the case where the objective function involves integration over space or time; in that case, the structure of η can have a profound effect on the calculated sensitivities. This paper analyzes a linear objective function at a single point in space and time. Considering a point in time allows investigation of the rapid barotropic response (storm surge or impulse response, lasting only a few hours) that is seen in tide gauge data, and that would be obscured by time averaging. The linear function avoids weighting by the forward model state values in the cost function. Most important for our goals, using a point in space and time as the objective function allows better visualization of the sensitivity propagation mechanisms and the dynamics involved.

Three adjoint runs have been analyzed for this work. In the first, y is defined as the SSH at $\mathbf{x} = (35.1°\text{N}, 120.8°\text{W})$ and $t = 0000$ UTC 1 February 2008. In the second, $t = 0000$ UTC 1 August 2008 and in the third, $t = 1200$ UTC 1 August 2008 (with $\mathbf{x}$ unchanged).

The primary analysis in this paper focuses on the sensitivity of SSH at Port San Luis to the surface wind stress ($f = \tau$). The wind stress vector (with zonal and meridional components τ_x and τ_y, respectively) is decomposed into cross- and alongshore components ($\tau_\perp$ and $\tau_\parallel$) by rotating the vector by an angle θ, corresponding to the orientation of the coastline. This is commonly done in studies of the California Current System with $\theta = 33°$ as the average orientation the central California coast (e.g., Veneziani et al. 2009). The local coastline at Port San Luis is variable such that it is not clear if $\theta = 33°$ is the proper rotation. Nevertheless, this average coastal orientation is used here, and the sensitivities to wind stress are rotated as such:

$$\frac{\partial J}{\partial \tau_\perp} = \frac{\partial J}{\partial \tau_x} \cos\theta + \frac{\partial J}{\partial \tau_y} \sin\theta \quad \text{and} \qquad (5)$$

$$\frac{\partial J}{\partial \tau_\parallel} = -\frac{\partial J}{\partial \tau_x} \sin\theta + \frac{\partial J}{\partial \tau_y} \cos\theta, \qquad (6)$$

which preserves the magnitude of the sensitivity. We also consider the sensitivity to surface heat fluxes ($f = Q$) and freshwater fluxes ($f = $ FW, given by the difference between precipitation and evaporation, plus river runoff).

To quantitatively compare the sensitivity of SSH to different components of forcing, sensitivities are weighted by a measure of typical variations in the corresponding forcing field (Veneziani et al. 2009):

$$dJ_f = \frac{\partial J}{\partial f} \sigma_f, \qquad (7)$$

where σ_f is the standard deviation (calculated at each grid point) of the departures from the seasonal cycle for the forcing component f. This scaling gives all sensitivities the same units (units of J), making them easily comparable, but the choice of σ_f reflects the uncertainty in f for the desired calculation, and can therefore vary with application. This has a controlling effect on the calculation, because zero uncertainty would therefore mean zero normalized sensitivity, but the choice must be justifiable. In this case it reflects uncertainty with respect to climatology, and is calculated the same way for all fields.

The adjoint is run backward in time for 100 days from the time of J (i.e., 1 February 2008 or 1 August 2008), such that sensitivities are calculated for time lags between forcing and response ranging from 0 to 100 days.

A caveat of the method is that the adjoint model is linearized around the forward model state. Thus, the adjoint-derived sensitivities are only accurate for small perturbations around the forward model state. The validity of the linearity assumption in MITgcm simulations can be verified through gradient checks and finite perturbation experiments (e.g., Losch and Heimbach 2007; Mazloff 2012). The fact that adjoint optimization can be employed to produce a multiyear state estimate (i.e., the cost function is reduced) implies that the linear method is useful over long periods of time. A perturbation experiment in the forward model, presented in the next section, confirms that nonlinearities in the response to finite wind stress perturbations remain small over the 100-day integration.

3. Coastal SSH response to a finite wind perturbation

The SSH response to wind stress fluctuations is probed by wind perturbation experiments in forward model runs. Quantifying the response to atmospheric forcing forward in time is more familiar and complements and aids interpretation of the adjoint sensitivity analysis presented in section 4. The experiment involves perturbing the alongshore wind stress near San Diego on 1 July 2007. The perturbation is Gaussian shaped with an amplitude $\sigma_{\tau_\parallel}$ of $0.1\,\mathrm{N\,m^{-2}}$ and an e-folding scale of $0.5°$, and is applied over 1 day (the wind stress increases from 0 to $\sigma_{\tau_\parallel}$ over 12 h, then decreases back to 0 over the

next 12 h; this is simulated as a Gaussian pulse with an e-folding scale of 6 h). The amplitude of this perturbation is chosen as representative of a typical wind event for the California Current System region [the NAM winds in coastal areas have a standard deviation ranging from 0.02 to $0.11\,\mathrm{N\,m^{-2}}$ depending on latitude, in agreement with Quick Scatterometer (QuikSCAT) winds from http://coastwatch.pfeg.noaa.gov/erddap/griddap/erdQSstress1day.html], though it is large for the specific location where the perturbation is applied (near San Diego, California, the NAM winds have a standard deviation of $0.021\,\mathrm{N\,m^{-2}}$, which is lower than the $0.035\,\mathrm{N\,m^{-2}}$ from QuikSCAT data).

The spatiotemporal evolution of the SSH perturbation is shown in Fig. 4. Daily averages are plotted, thus emphasizing the baroclinic response, as the fast barotropic response is smoothed by the averaging. It illustrates the regional dynamics taking place during the response to a positive perturbation (weakening of the poleward-flowing alongshore winds). Initially, the anomalous winds push water toward the coast, resulting in an anomalous tilt in the sea surface. The anomalous SSH excites coastally trapped waves that propagate northward, and Rossby waves that propagate westward and slowly dissipate.

Comparing forward model perturbation experiments forced by identical positive and negative wind stress perturbations tests the validity of the adjoint linearity assumption. We carry out a second experiment where the perturbation amplitude is negative (i.e., $\sigma_{\tau_\parallel} = -0.1\,\mathrm{N\,m^{-2}}$). The SSH differences from the reference and the perturbation simulations are $\delta h_1 = (h_+) - h_0$ and $\delta h_2 = (h_-) - h_0$, where h_+ is the SSH with the positive perturbation, h_0 is the SSH in the control model run, and h_- is the SSH with the negative perturbation. The SSH differences can be combined into first and second derivative estimates: $\delta H_1 = (\delta h_1 - \delta h_2)/2$ and $\delta H_2 = (\delta h_1 + \delta h_2)/2$. At every point, the differences between the perturbed and the control simulation can be expressed as a Taylor expansion in powers of the perturbation. The first term is linear, the second is quadratic, and so on. The δH_1 includes the linear response, third-order nonlinear term, and higher-order (odd) terms. The second difference, δH_2, includes even-order terms, and is an approximate indicator of when the first nonlinear term in the expansion becomes important. When $\delta H_1 \gg \delta H_2$, the even nonlinear terms are small and δH_1 is likely to be an adequate approximation of the linear response. When the two are comparable in magnitude, further investigation of the high-order terms is required, and δH_1 may not be representative of the linear response.

The evolution of δH_1 and δH_2, expressed by taking their root-mean-square (RMS) over an area surrounding the wind perturbation ($32°$–$34°$N, $117°$–$119°$W), is shown
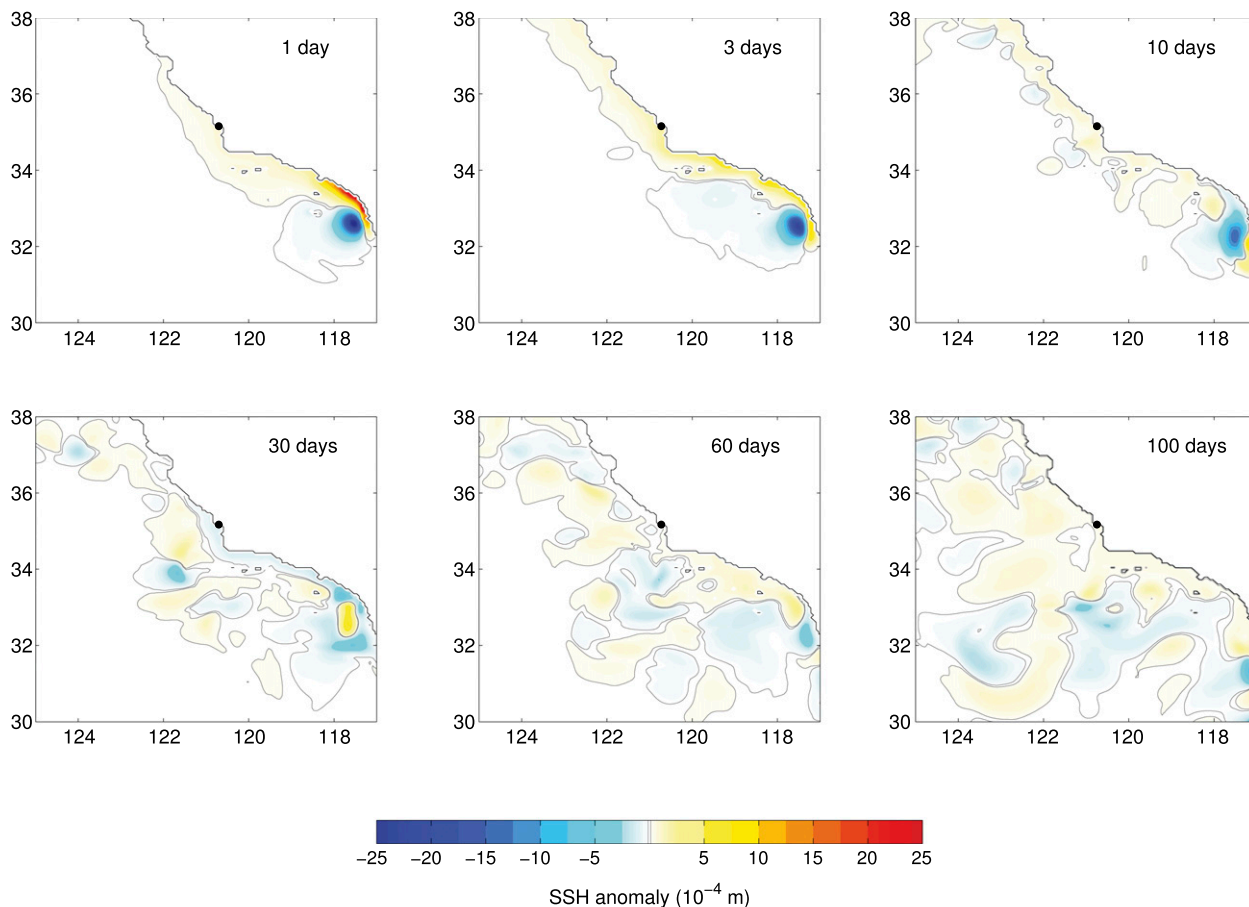
FIG. 4. Snapshots of the SSH response to a wind perturbation applied on 1 Aug 2008, in the forward model. The response is shown for $t =$ 1, 3, 10, 30, 60, and 100 days after the end of the perturbation.

in Fig. 5. Throughout the 100-day simulation, the RMS of the nonlinear response is small compared to the linear response. Thus the modeled response to the $0.1 \, \mathrm{N \, m^{-2}}$ wind stress anomaly analyzed, which is an anomaly of typical magnitude for the region, is largely linear.

The relatively small magnitude of the SSH response is due to the short temporal duration (1 day) and small spatial extent (~7 km) of the perturbation. For the wind perturbation of $0.1 \, \mathrm{N \, m^{-2}}$, the largest SSH anomaly occurs near the perturbation and reaches 0.002 m (Fig. 4). Increasing the magnitude of the perturbation causes a larger SSH anomaly, and a more nonlinear response. For a (huge) wind stress anomaly of $1 \, \mathrm{N \, m^{-2}}$ applied over the same area and the same period of time, the local SSH anomaly reaches 0.015 m. In that case, the magnitude of δH_2 becomes comparable to the magnitude of δH_1 after about 20 days (not shown). Increasing the duration of the perturbation 20-fold has a similar effect. Thus, the (linear) adjoint-derived sensitivities presented in the next section are good approximations to the true sensitivities over long time scales (100 days) as long as the

perturbation is small, such as a typical wind anomaly lasting 1 day. However, for large perturbations, the sensitivities should be interpreted cautiously for time scales longer than a few weeks, as nonlinear effects become significant.

4. Adjoint sensitivity of coastal SSH to atmospheric forcing

In this section, the results of adjoint sensitivity experiments are presented. First, the spatial and temporal patterns of SSH sensitivity to atmospheric forcing are described. The SSH response is then reconstructed from the sensitivities and the forcing; this hindcast offers additional support of the validity of the adjoint method. Finally, spectral characteristics of the sensitivities are presented.

a. Spatial and temporal structure of the sensitivities

Insight into the physics is gained by examining the spatial patterns of sensitivities and their evolution in
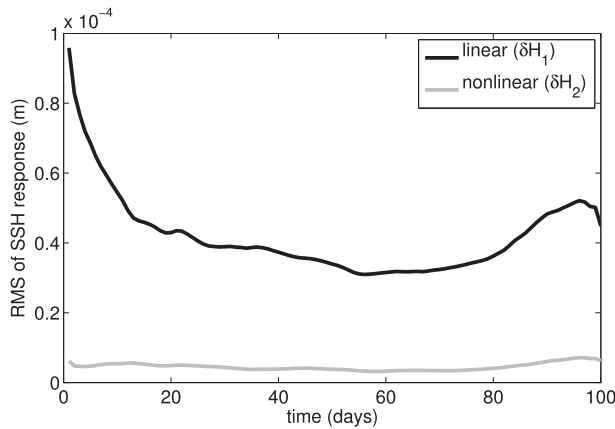
FIG. 5. Linear (black) and nonlinear (gray) SSH response to a finite wind perturbation in the forward model. The alongshore wind stress is perturbed by $\pm 0.1\,\mathrm{N\,m^{-2}}$ over 12 h and then brought back to the control value over the next 12 h; this perturbation is applied over a $1° \times 1°$ area near San Diego. The linear response is approximated by the difference between the SSH anomalies resulting from the positive and negative perturbations, and the nonlinear response by their sum (see text for more details).

time. Figure 6 shows selected snapshots of the weighted sensitivity to wind stress ($dJ_{\tau_\perp}$ and $dJ_{\tau_\parallel}$) during the 36-h period leading to the SSH response. Each map shows the forcing that can drive the coastal SSH response at the later time. A positive (negative) sensitivity implies that a positive wind perturbation at that location will cause a positive (negative) change in SSH at Port San Luis. The sensitivity is largest at the tide gauge, but is nonnegligible over a large fraction of the domain. Though sensitivity magnitudes are similar, there are obvious structural differences between the influence of cross- and alongshore winds on coastal SSH. On short time scales, cross-shore winds pile water up at the coast resulting in an SSH rise, as shown by the strong sensitivity offshore of Port San Luis. In contrast, with alongshore winds it is the convergence of the transport that initially matters most. In both cases, the initial effect is reversed an hour later (cf. the snapshots at hours 1 and 2) because of oscillations of the displaced sea surface. There is a relatively large sensitivity to the winds in the Sebastián Vizcaíno Bay at the southern end of the domain, which alternates between positive and negative and disappears after about 12 h. This likely indicates a resonance phenomenon originating in the bay.

After 24 h, wavelike sensitivity patterns start to develop offshore. The period of oscillation varies between 0.6 and 0.9 day, which is similar to the inertial period near Port San Luis (0.87 day). When surface winds drive near-inertial motions in the mixed layer, horizontal convergence can occur, which leads to the generation of

internal waves (e.g., D'Asaro et al. 1995; MacKinnon and Gregg 2005). Time-varying winds can efficiently inject kinetic energy into the near-inertial band of the internal wave spectrum (Alford 2003). Near-inertial waves can propagate onto the continental shelf (e.g., Shearman 2005; MacKinnon and Gregg 2005; Sobarzo et al. 2007), carrying the effects of offshore winds to the coast (Fig. 7).

Sensitivities along the coast south of Port San Luis are indicative of coastally trapped waves (Figs. 6 and 7). The sensitivities extend farther southward as the time lag increases, indicating a physical mechanism propagating the effects of the forcing northward. From Fig. 7, it is inferred that the signal propagates at a speed of up to $6\,\mathrm{m\,s^{-1}}$ and extends 50–100 km offshore. These values are consistent with the length scale and phase speed of coastally trapped waves, which are a mixture of Kelvin and shelf waves (Gill 1982).

While Fig. 6 shows the August sensitivities, the patterns are nearly identical for the February sensitivities. For the longer evolution of sensitivities (Fig. 7), the patterns are qualitatively very similar for August and February sensitivities, although the amplitude is different. The February sensitivities decay faster, especially near the tide gauge and offshore of Port San Luis. The difference is due to seasonal variations in the forward model ocean state, especially the stratification, as discussed in section 5b. Even in the August case, sensitivities have decayed significantly by day 30 (Fig. 7), and remain weak over the 100 days analyzed (not shown). Forward perturbation experiments (not shown) verified these seasonal differences.

The total sensitivity of SSH to atmospheric forcing is the cumulative effect of sensitivities to each forcing component (alongshore winds, cross-shore winds, heat fluxes, and freshwater fluxes). These multiple time series of two-dimensional sensitivity maps are voluminous, and there is a need for simpler summary statistics. Because positive and negative sensitivities are possible, a meaningful measure of the integrated sensitivity ideally accounts for the magnitude of sensitivity components, rather than just their net sum (Zhang et al. 2012). One option is to use the quadratic mean, or RMS, as a measure of the total sensitivity. However, this nonlinear measure is not well suited to calculations that involve partitioning the sensitivities, such as between the different components of forcing, or between local and remote forcing. Instead, we define two measures of the total sensitivity. One sums in time the absolute value of the spatial mean sensitivity for each component (dJ_{mean}); the other sums in time the spatial mean of the absolute values (dJ_{var}). These can be written as

FIG. 6. Snapshots of the sensitivity of SSH on 1 Aug 2008 to (a) along- and (b) cross-shore wind stress over a 36-h period. Sensitivities are weighed by the spatially varying std dev of the wind stress. The time lag between wind perturbation and SSH response is indicated in each box. These maps show the forcing that can drive the coastal SSH response. A positive (negative) sensitivity implies that a positive wind perturbation at that location will cause a positive (negative) change in SSH at Port San Luis. A logarithmic color scale is used; only sensitivities exceeding the threshold (2.5×10^{-9} m) are colored.

a) alongshore wind stress

b) cross−shore wind stress

FIG. 7. As in Fig. 6, but for a longer time scale (2–30 days).

$$dJ_{\mathrm{mean}} = |\langle dJ_{\tau_\perp}\rangle| + |\langle dJ_{\tau_\parallel}\rangle| + |\langle dJ_Q\rangle| + |\langle dJ_{\mathrm{FW}}\rangle|$$

and $\qquad\qquad\qquad\qquad\qquad\qquad$ (8)

$$dJ_{\mathrm{var}} = \langle|dJ_{\tau_\perp}|\rangle + \langle|dJ_{\tau_\parallel}|\rangle + \langle|dJ_Q|\rangle + \langle|dJ_{\mathrm{FW}}|\rangle, \quad (9)$$

where averages (indicated by angle brackets) are taken over the spatial domain (up to 1° away from open boundaries). Total sensitivities are summed over the 100 days of adjoint integration.

These two metrics provide complementary information on the total sensitivity. Here, dJ_{mean} quantifies the effect of spatially uniform (basin scale) forcing perturbations, while dJ_{var} is a metric of the magnitude of spatially varying sensitivities. For example, the sensitivity to alongshore winds is large (leading to a large dJ_{var}), but to realize the potential response would require winds with small-scale structure (either concentrated in areas with sensitivities of similar sign, or with a spatial pattern that matches that of sensitivities); a spatially uniform wind stress perturbation will produce a small response (as quantified by the small dJ_{mean}). In practice, of course, atmospheric forcing is neither exactly uniform nor does it exhibit such a small-scale structure as seen in the sensitivities (Fig. 7), and care must be taken in interpreting the metrics.

The relative contribution of the different components of forcing to dJ_{mean} and dJ_{var} is summarized in Table 2. Although the two metrics give different values, both indicate that alongshore wind is the dominant component (86% of the sensitivity to a uniform forcing and 63%–69% of the sensitivity to spatially varying forcing, depending on season). Cross-shore winds account for a small fraction of the sensitivity to a uniform forcing (1%–10%), but a larger fraction of the sensitivity to spatially varying forcing (21%–23%). The remaining sensitivity comes from heat fluxes and freshwater fluxes.

The sensitivity can also be partitioned into local and remote contributions (Fig. 8). The short- and long-term responses are emphasized by looking at the cumulative sum of dJ_{mean} and dJ_{var} over the time of adjoint integration. Only the sensitivities to wind stress are included here, because steric effects propagate and dissipate via different dynamics and persist on much longer scales in time and space. The domain is split into three regions for analysis: local, coastal (nonlocal), and offshore (see Fig. 1). The local region is defined as the area within 100 km of Port San Luis. The coastal region is defined as the area where ocean depth is less than 1500 m (excluding the local area). The remaining area is considered offshore. The relative contribution from each region is scaled by the corresponding area.

TABLE 2. Attribution of the total sensitivity (measured as dJ_{mean} or dJ_{var}) to the four components of atmospheric forcing.

		$\tau_\parallel$	$\tau_\perp$	Q	FW
dJ_{mean}	Feb	86%	8%	4%	2%
	Aug	86%	1%	10%	3%
dJ_{var}	Feb	63%	21%	11%	5%
	Aug	69%	23%	6%	2%

Local winds dominate the short-term response, whereas the effect of nonlocal winds accumulates more slowly (Fig. 8). The sensitivity to uniform forcing is largely local, with the nonlocal contribution being split almost equally between coastal and offshore winds. In February nonlocal effects exceed the local contribution after about 3 weeks, but in August local effects remain dominant. The sensitivity to spatially varying forcing is dominated by nonlocal winds after only 1 day, and the offshore contribution is approximately twice as large as the coastal contribution. This is explained by the presence of small-scale structures in the sensitivity, especially offshore (due to inertia–gravity waves). The potential for optimal excitation of these wave patterns makes dJ_{var} exceed dJ_{mean} by an order of magnitude. Winds are not likely to exhibit such an optimal small-scale structure and this optimum sensitivity regime is not expected to be fully realized; indeed, the hindcast reveals that offshore winds contribute less to SSH variability than coastal winds (see section 3b). Over the 100-day period, the fraction of dJ_{var} that is attributed to local winds is 13% in February and 19% in August. Thus, in both seasons, the cumulative effect of nonlocal winds accounts for more than 80% of the total sensitivity emphasizing connectivity and the potential for nonlocal effects to propagate via excitation of wave dynamics. The relative contribution of coastal winds is slightly larger in February (21%) than in August (18%), and the same is true for offshore winds (66% in February and 62% in August). Overall, the total sensitivity in summer is greater than in winter, because local and offshore sensitivities decay more rapidly in February, whereas they persist in August, because of the lower winter stratification (see section 5b).

To emphasize the seasonal differences, sensitivities are normalized by the cumulative value at day 100 and compared (Fig. 9). When considering the entire domain, both the dJ_{var} and dJ_{mean} sensitivity metrics approach the final total faster in February. The evolution of sensitivities at the four specific locations marked on Fig. 1 (a point near Port San Luis, a point offshore, a point on the coast near San Diego, and a point in Sebastián Vizcaíno Bay at the southern end of the domain) clearly show that in February the effect of local and offshore winds becomes small after ~20 days, whereas in August
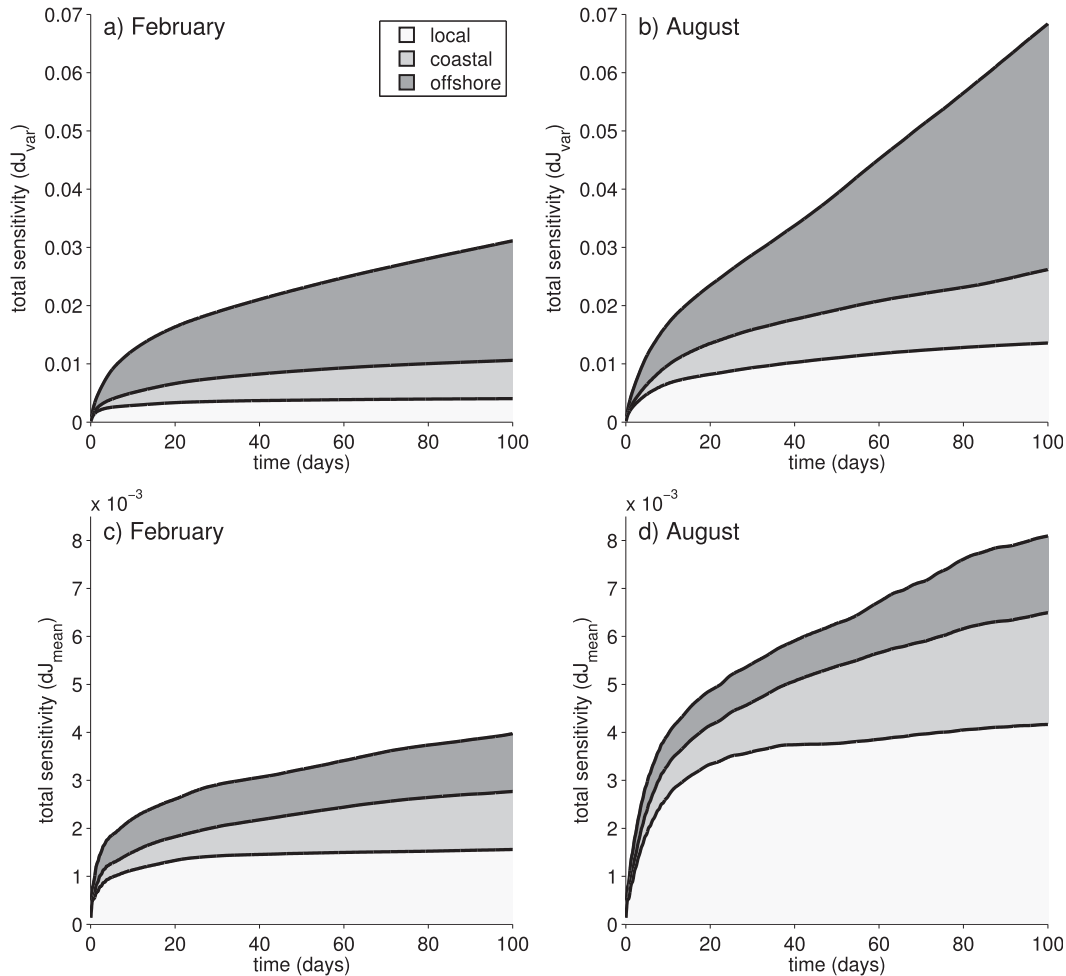
FIG. 8. Cumulative sum of the total sensitivity, as defined by the metrics (a),(b) dJ_{var} and (c),(d) dJ_{mean} for February and August. Only along- and cross-shore wind stress are included in the calculation (steric effects are excluded). Contributions from local and nonlocal sources are shown as different shades of gray. The local, coastal, and offshore regions are shown in Fig. 1.

it remains nonnegligible throughout the 100-day simulation. In contrast, winds blowing over the bay and along the coast (equatorward of Port San Luis) have similar effects in February and August.

Figure 9d highlights the effects of barotropic and baroclinic coastally trapped waves. Rapidly propagating barotropic waves carry the effects of wind perturbations over the bay in less than a day. Farther north, the contribution from barotropic coastally trapped waves appears to be negligible (Fig. 9c). This suggests that barotropic waves are amplified in the bay through some resonance mechanism. Contributions from slower baroclinic coastally trapped waves persist over several months. Their effect builds up more slowly in February, which is consistent with a slower phase speed for Kelvin waves in a less stratified ocean.

b. Hindcasting with adjoint-derived sensitivities

Adjoint sensitivities provide insight on how the different forcing components have the potential to contribute to SSH variability. However, the realized variability depends not only on sensitivity, but also on the forcing itself. During a given period of time, forcing components can be weak, or positive and negative contributions to SSH variability from these forcing components may offset each other, thus leading to a smaller effect on SSH variability than predicted by looking simply at sensitivities. To provide a more practical measure of influence, a hindcast is performed that reconstructs the response (i.e., J) by integrating the product of the sensitivity $(\partial J/\partial f)$ and the changes in forcing (Δf) over space and time. This allows quantification of the contribution of each forcing
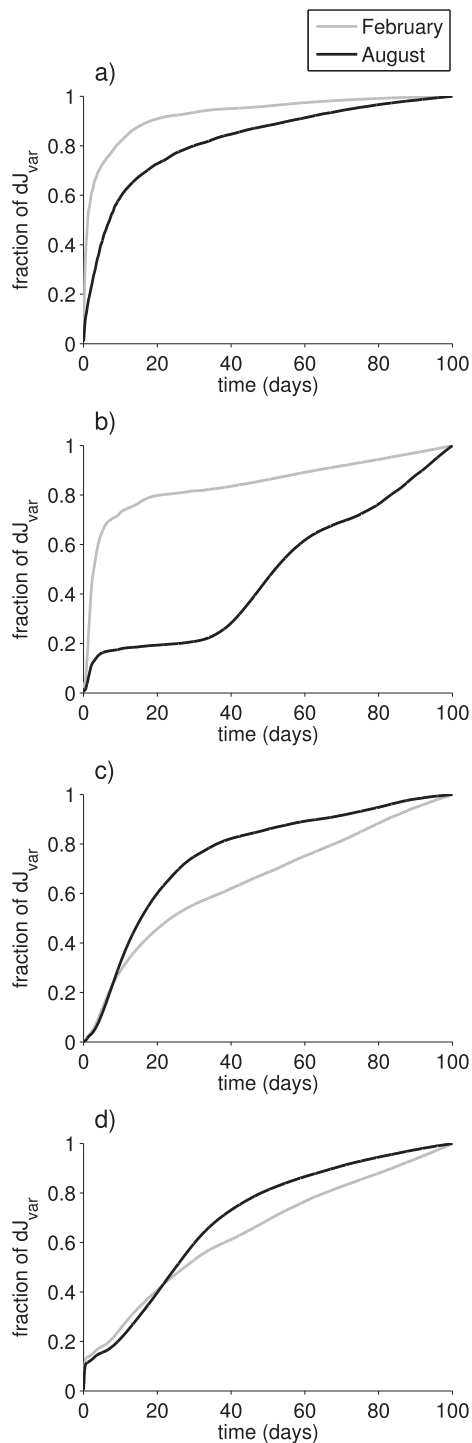
FIG. 9. Normalized cumulative sum of the total sensitivity, as defined by the metrics dJ_{var} for February (gray) and August (black) at four locations. Only along- and cross-shore wind stresses are included in the calculation (steric effects are excluded). All curves are normalized by the value at $t = 100$ days. Sensitivities are averaged over a 0.5° square area around each location: (a) near Port San Luis, (b) offshore ~250 km southwest of Port San Luis, (c) on the coast to the south of Port San Luis, and (d) in the bay at the southern end of the domain (in Fig. 1 these locations are marked A, B, C, D, respectively).

component. For example, for $J = \eta$ at time t, the contribution of alongshore winds to SSH variation is the product of the variation in alongshore wind stress and the sensitivity of SSH to alongshore wind stress, integrated over all space and earlier times:

$$\Delta \eta_{\tau_{\parallel}}(t) = \int_{\mathbf{x}'} \int_{t'<t} \frac{\partial J}{\partial \tau_{\parallel}}(\mathbf{x}', t - t') \Delta \tau_{\parallel}(\mathbf{x}', t - t') \, dt' \, d\mathbf{x}'.$$

(10)

Summing over all forcing components (along- and cross-shore wind stress, heat fluxes, and freshwater fluxes) gives the total SSH variation at that time:

$$\Delta \eta(t) = \Delta \eta_{\tau_{\parallel}}(t) + \Delta \eta_{\tau_{\perp}}(t) + \Delta \eta_Q(t) + \Delta \eta_{FW}(t). \quad (11)$$

Given that the model output is discrete in time and in space, with a spatial resolution corresponding to the model grid and a 6-h temporal resolution, the integration in Eq. (10) must be discretized as well. If the model was linear and sampled at high enough temporal resolution, the hindcast would correspond exactly to the value of J. Thus, the hindcast also serves as a test of the adjoint and the linearity assumption.

Assuming that sensitivities depend only on time lag and not on the actual time of the objective function calculation allows one to hindcast SSH variations given knowledge of the forcings. The time integral in Eq. (10) then becomes a convolution. Using the model forcings and the sensitivity of SSH determined in August does indeed produce a hindcast that captures most of the variability in the simulated SSH time series (Fig. 10a). Daily averaging the 6-hourly hindcast and comparing to the daily-averaged simulated SSH yields a correlation coefficient of 0.81. Discrepancies in the hindcast and simulated SSH are explained partly by the seasonal variations in the sensitivities, which are not taken into account in this hindcast (only August sensitivities are used). Other sources of differences include nonlinearity, coarse time sampling aliasing the fast response with 6-h sampling of the sensitivities, and numerical noise. Barotropic inflow originating outside the model domain sets the rate of domain-mean sea level change, and thus induces variability in coastal SSH. This implies sensitivity to open boundary conditions, which is not included in the hindcast. The effects of the barotropic inflow were removed by subtracting the domain-averaged SSH from the local SSH at every time step.

Truncating the convolution in time (i.e., integrating from δt to t, where δt varies from 0 to 100 days) shows the time scale of the contributions to the hindcast. This calculation reveals how the forcing components
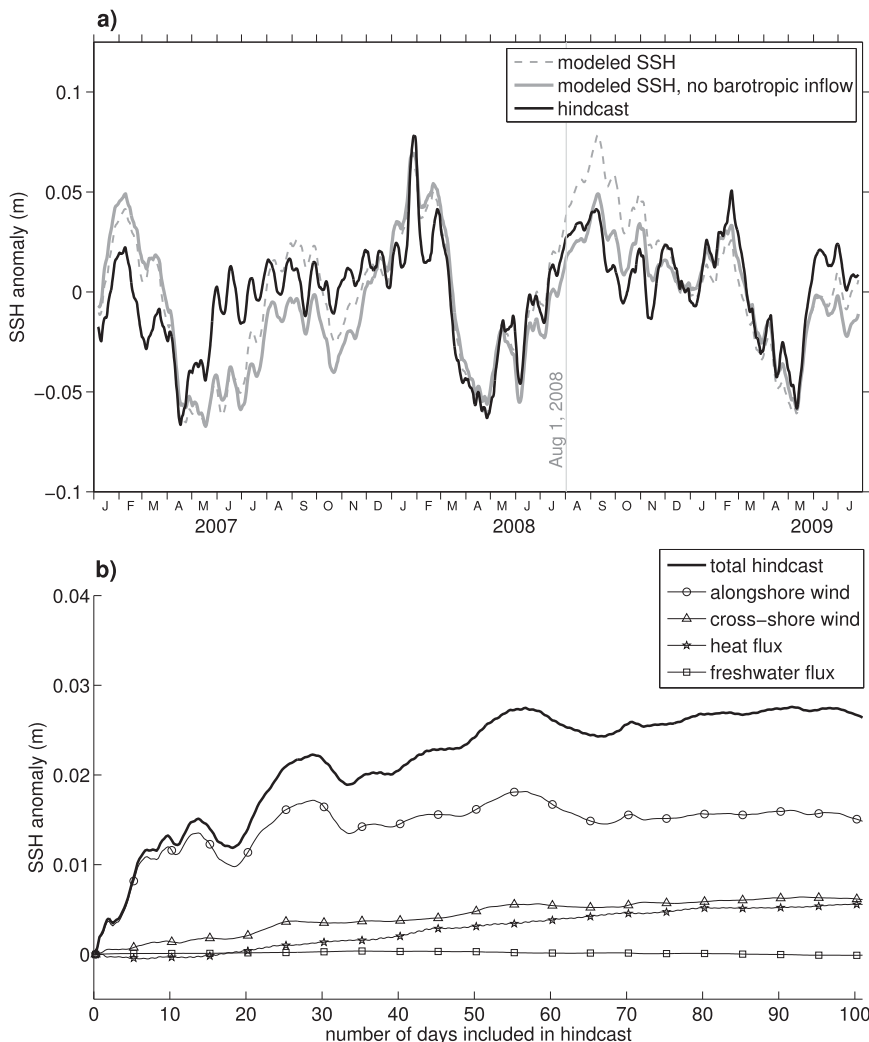
FIG. 10. Hindcast of SSH at Port San Luis calculated from the sensitivities to atmospheric forcing on 1 Aug 2008. (a) Hindcast (black), modeled SSH (dashed gray), and SSH without barotropic inflow (solid gray; see text for explanation). A 10-day running mean is applied to all time series. The vertical line indicates 1 Aug 2008. (b) Cumulative contribution from each of the forcing components ($\tau_\parallel$, $\tau_\perp$, Q, and FW) to the hindcast for 1 Aug 2008.

contribute to the SSH signal over in time. It is shown for the hindcast of SSH on 1 August 2008 in Fig. 10b. Alongshore winds account for the largest fraction of the SSH response, with significant contributions from cross-shore winds and heat fluxes. Freshwater fluxes have a negligible contribution to the SSH signal. The timing of the response varies between forcing mechanisms. Most of the response to alongshore winds occurs within 10 days. However, the response to cross-shore winds takes about 100 days to accumulate. The response to steric effects continues to build up even after 100 days. The differing behavior is expected because the kinetic energy input by the wind is eventually dissipated by viscosity, but steric changes are not subject to the same

decay mechanisms, and can persist for much longer durations.

When the calculation is repeated using the sensitivities for February, the hindcast similarly captures the timing of SSH variations, but the magnitude is underestimated (not shown). This is to be expected because the short-term sensitivities are the same, and the long-term sensitivities are qualitatively similar, only weaker in February. This suggests that the SSH variability is largely controlled by the short-term response, which in turn is dominated by the response to alongshore wind stress.

The hindcast was decomposed into parts driven by local, coastal, and offshore winds, and the contributions from these components to the full hindcast variability

TABLE 3. Statistics of the hindcast realized with different winds: std dev σ, correlation with the modeled SSH ρ_{SSH}, and correlation with the total hindcast $\rho_{\Delta\eta}$. Each column is for a different hindcast that includes only the contribution from winds that are either local $\Delta\eta_{\mathrm{local}}$, coastal $\Delta\eta_{\mathrm{coastal}}$, offshore $\Delta\eta_{\mathrm{offshore}}$, or the sum of all winds $\Delta\eta$ (=$\Delta\eta_{\mathrm{local}} + \Delta\eta_{\mathrm{coastal}} + \Delta\eta_{\mathrm{offshore}}$). February and August sensitivities are used separately in the hindcast calculation. Heat and freshwater flux forcing are not included.

		$\Delta\eta_{\mathrm{local}}$	$\Delta\eta_{\mathrm{coastal}}$	$\Delta\eta_{\mathrm{offshore}}$	$\Delta\eta$
σ	Feb	7.0	9.1	4.3	18.5
	Aug	14.8	11.2	5.0	29.5
ρ_{SSH}	Feb	0.72	0.87	0.74	0.87
	Aug	0.80	0.81	0.73	0.87
$\rho_{\Delta\eta}$	Feb	0.90	0.95	0.83	1
	Aug	0.93	0.93	0.78	1

are summarized in Table 3. This result confirms that both local and nonlocal winds are important drivers of coastal SSH variability. The contribution from offshore winds is weaker than anticipated based on the measures dJ_{mean} and dJ_{var}. This suggests that, in addition to the small-scale spatial variability in offshore sensitivity, there is also high-frequency temporal variability in the sensitivity to forcing. Indeed the sensitivities offshore oscillate in time, and the effect of a long-lasting wind event will partially cancel by generating inertia–gravity waves that act on SSH with different phases.

Interestingly, the hindcasts realized with only local, coastal, or offshore winds are all highly correlated with modeled SSH (Table 3). This is explained by a high spatial autocorrelation of the surface wind stress in the California region. Local and remote winds tend to enhance each other's effect on coastal SSH, such that each component of the hindcast is often in phase with the total hindcast. While the coastal winds hindcast has the highest correlation with modeled SSH, coastal winds themselves cannot account for the magnitude of SSH variability. Local and offshore winds are responsible for at least half of the variability in the total hindcast.

c. Spectral characteristics of the sensitivities

There is growing appreciation of how transfer functions can be used as a model diagnostic (e.g., Kim et al. 2009; MacMynowski and Tziperman 2010). These frequency-dependent linear relationships between in- and output were calculated here using Fourier transforms of the hourly time series of adjoint-derived sensitivities. The amplitude of transfer functions for local winds is shown in Fig. 11. Each gray curve corresponds to a single grid point in a $0.5° \times 0.5°$ area near the tide gauge. The thick black curve is the average over that area. Peaks at a period of 0.87 days, the inertial period, indicate the effect of near-inertial waves. In August, there is an additional

peak at a period of 1 day. This peak it not well separated from the inertial peak, and is most apparent close to the tide gauge location. It is caused by diurnal variations in mixed layer thickness, which modulates the sensitivities, with SSH being less sensitive to winds blowing at night (over a deeper mixed layer). This effect is more noticeable in summer, when the diurnal variation is a significant fraction of the shallow MLD. Shifting the objective function by 12 h confirms that the phase of oscillations in the sensitivity is determined by the time of day, not by the time lag relative to the objective function.

The transfer function amplitude is small at periods of a few hours meaning this high-frequency forcing is unable to drive a strong response. (Forcing at a higher frequency than a response cancels itself netting a vanishing effect.) The transfer functions flatten at periods between 10 and 100 days indicating that the time scale of the forcing exceeds that of the response. At these low frequencies, the forcing is essentially constant or unidirectional. (The period at which the transfer function flattens out indicates the maximum time scale of the response, such that forcing at periods longer than that time scale will yield the same response.) Peaks in the transfer function, here noticeable at the inertial period, indicate resonance.

Figure 12 shows transfer functions for winds from four locations (marked on Fig. 1, the same as in Fig. 9). For local and offshore winds, the February and August transfer functions are similar at short periods but diverge for longer periods. This indicates that the short-term response (1–2 days, see Fig. 6) is the same for the two seasons (i.e., it is unaffected by stratification). The response to low-frequency winds has a lower amplitude in February, when the mixed layer is deep, than in August, when the mixed layer is shallow (consistent with the results from section 4a).

In contrast, the coastal transfer functions at the San Diego and Sebastián Vizcaíno Bay locations do not exhibit notable seasonal differences. These transfer functions are still increasing at a 100-day period, suggesting that coastal winds have very long-lasting effects (that are carried by baroclinic coastally trapped waves). There is a peak at a period of 4 h in the response to winds in the Sebastián Vizcaíno Bay, reflecting the fast barotropic resonance seen in Fig. 6.

5. Discussion

a. Propagation of sensitivities

The adjoint calculations shown here provide a detailed look at the physical pathways linking the SSH response at a point to the atmospheric forcing elsewhere. In particular, significant influence is seen to pass through the
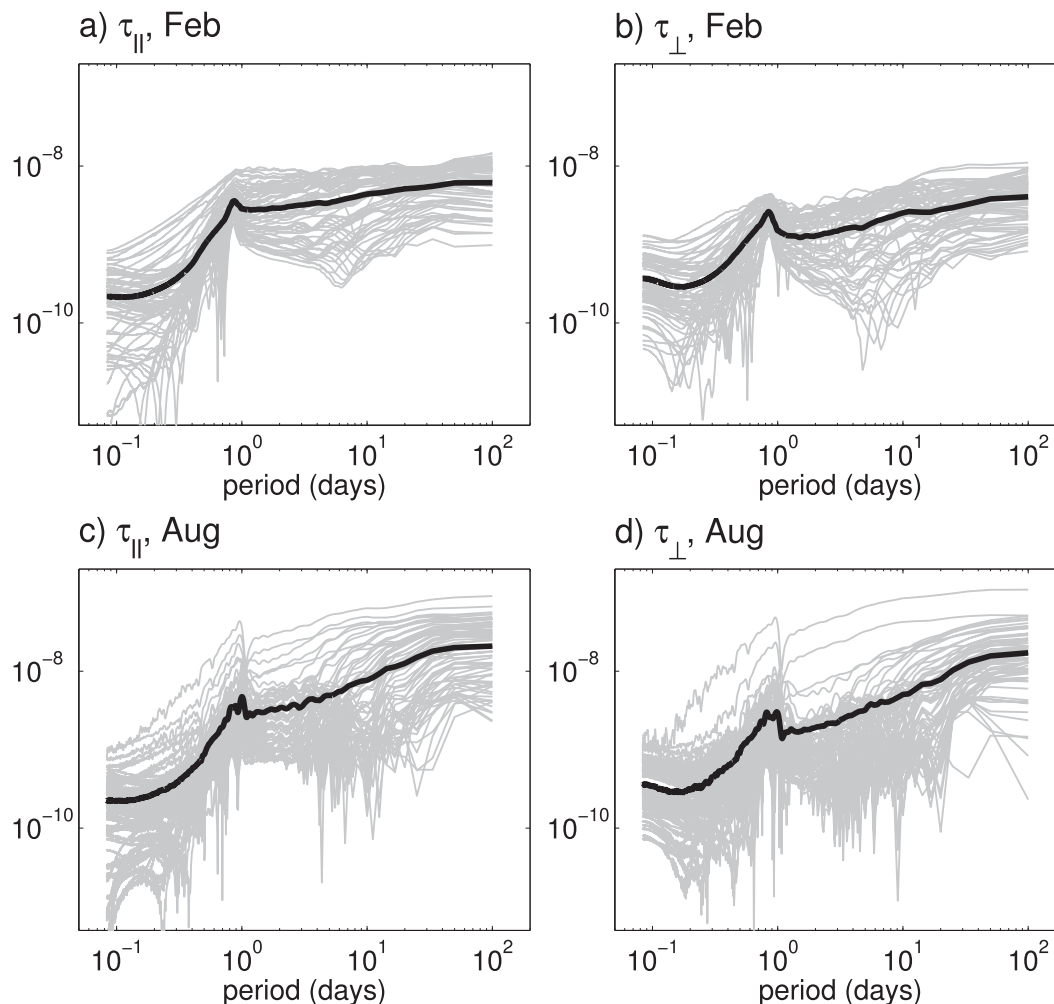
FIG. 11. Amplitude of the transfer function for along- and cross-shore wind stress in (a),(b) February and (c),(d) August. Each gray curve is for one grid point in a 0.5° square area near Port San Luis; black curves show the average spectra. Transfer functions are obtained by taking the Fourier transform of sensitivity time series. There is a peak at the inertial period, $T = 0.87$ days, in both seasons. There is also a peak at $T = 1$ day in summer due to the diurnal cycle in the mixed layer.

Southern California Bight and around Point Conception. The short-time response shows characteristics of storm surge, and some interesting resonances in a bay in Baja California, while the long-term response shows the baroclinic dynamics. This extends the work of Veneziani et al. (2009) to both shorter and longer time scales, and uses a more local cost function and more time sampling for less blurring of the propagation features.

The response to wind stress reflects the transfer of momentum directly to the mixed layer during the first few hours. At time scales beyond a few hours the effects of rotation are seen, such as Ekman dynamics including inertia–gravity waves and propagation of barotropic Rossby and coastally trapped waves, which are insensitive to the stratification. On still longer time scales, the

response shows propagation of baroclinic Rossby and coastally trapped waves and other wind-induced motions in the mixed layer at the coast. Coastally trapped waves are easily identified by the poleward propagation of the effect of coastal winds (Gill 1982).

Inertia–gravity waves are identified from the oscillating sensitivities offshore of Port San Luis. Such oscillations indicate that time-varying winds can efficiently inject kinetic energy into the mixed layer in the near-inertial-frequency band and that these motions can produce SSH changes at the coast. The local wind-driven response likely involves the generation of near-inertial currents and vertical propagation of internal waves, as described in MacKinnon and Gregg (2005). Most of these processes are, in different ways, affected
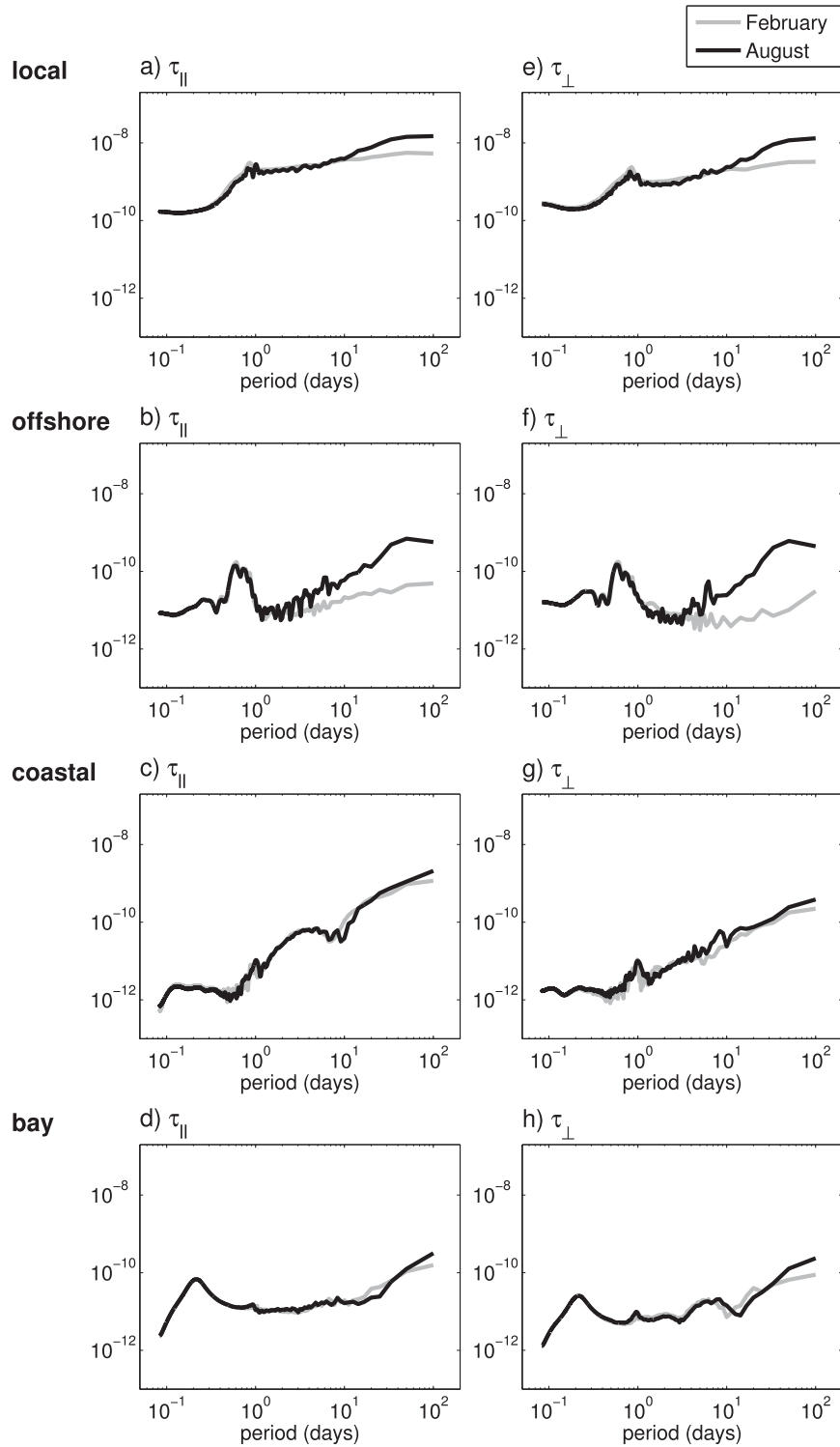
FIG. 12. Amplitude of the transfer function for (a)–(d) along- and (e)–(h) cross-shore wind stress at four locations (local, offshore, coastal, and in a bay) in February (gray) and August (black). Transfer functions are averaged over a 0.5° square area around each location marked A, B, C, and D in Fig. 1.

by stratification, leading to large seasonal variations in the sensitivities.

b. Seasonal dependence of sensitivities

After the initial response, which is the same in summer and winter, sensitivities evolve differently depending on the season. The long-term response, examined here over a period of 100 days, decays more rapidly in winter due to seasonal variations in the forward model ocean state. While the spatial patterns are similar, the contributions from local and offshore winds persist for longer times in August than in February, leading to overall higher sensitivity of SSH in August.

Changes in stratification affect the decay of wind-induced currents in the upper ocean. The mixed layer around Port San Luis is 2–3 times deeper in winter (∼70 m) than in summer (∼30 m). These deeper turbulent mixed layers distribute the wind input of momentum over greater depths. As a result there is a seasonal cycle in near-inertial kinetic energy, and an inverse relation between near-inertial surface currents and mixed layer depth (Shearman 2005). Internal waves provide a primary pathway for turbulent dissipation of this kinetic energy (MacKinnon and Gregg 2005). On the continental shelf, the enhanced connectivity to topography in winter increases the rate of momentum dissipation, resulting in a faster decay rate of the sensitivity to local and offshore winds. In contrast, the sensitivity to remote coastal winds does not appear to vary seasonally (Fig. 9), suggesting that the MLD does not significantly increase the damping of coastally trapped waves. However the waves appear to propagate more slowly in winter (Fig. 9) as a consequence of the lower stratification.

Diurnal changes in stratification are also found to impact the sensitivities. In summer, diurnal variations are significant compared to the mean MLD, and the magnitude of the sensitivity to local winds reflects this periodic change in stratification. The sensitivity of winds near the gauge location is modulated by oscillations with a period of 1 day (see Figs. 11c,d). The sensitivity to nighttime winds is smaller than the sensitivity to daytime winds; this is confirmed by experiments changing the time of the objective function by 12 h. Thus, the modulation of the response by the diurnal cycle produces oscillations in the sensitivity of coastal SSH, the sensitivity being larger when the water column is more stratified. As with the seasonal dependence, this diurnal variation does not apply to the short-term response, which is insensitive to stratification.

Two measures of the domain-wide sensitivity are used to quantify the evolution of the sensitivities over time. The first, dJ_{mean}, gives the response to uniform forcing; the second, dJ_{var}, is indicative of the response to spatially varying forcing. Both metrics show that the cumulative sensitivity after 100 days is twice as large in summer as it is in winter. Transfer functions indicate that the response to coastal winds exhibits little seasonal dependence. This implies that the generation of coastally trapped waves is weakly affected by stratification, as one expects because these waves originate as surface elevation changes in response to winds at the coast (this mechanism is bound to the surface region and does not involve ocean interior). In contrast, the long-term response to local and offshore winds varies strongly depending on the season, indicating that the mechanism carrying the effect of the wind stress is more complex and involves interactions with the ocean interior (not confined to the surface).

c. Dominance of alongshore winds

The effects of different components of forcing are quantified by their expected contributions to dJ_{mean} and dJ_{var}. Both measures attribute the largest fraction of the total sensitivity to alongshore winds, with cross-shore winds, heat fluxes, and freshwater fluxes playing lesser roles. This is consistent with the results of Veneziani et al. (2009) who also find the sensitivity to alongshore wind stress to be the dominant component. The hindcast of SSH on 1 August 2008 gives an alternative way of evaluating the relative contributions (section 4b). The growing responses over time reveal that the short-term response is almost entirely attributed to alongshore winds. The longer-term response is partitioned between alongshore winds, cross-shore winds, and heat fluxes.

d. Local versus remote winds

The largest sensitivities to wind stress occur near the location of the tide gauge. However, the effect of these local winds tends to be relatively fast with most of the sensitivity occurring within a week in summer, and within just a few days in winter (Figs. 6 and 7). The sensitivity to nonlocal winds is weaker, but longer lasting and more widely distributed over the domain. Thus, the remote forcing accounts for a large component of the total sensitivity (integrated over space and time). Remote forcing can be attributed to coastal winds, this effect propagating up the coast via coastally trapped waves, and to offshore winds, this effect propagating via inertia–gravity waves.

The sensitivity to offshore winds is large, especially in summer, indicating the potential to drive significant coastal SSH variability. It is noteworthy, however, that much of the sensitivity has small-scale spatial structure, and the effects will cancel out under large-scale wind patterns. In the hindcast driven by NAM winds, offshore winds have a small effect on coastal SSH variability. This

indicates that although the effect of wind-generated mixed layer motions offshore can reach the coast on time scales as long as 100 days or more, the contribution from winds in different locations and at different times tend to cancel each other.

Using coastal observations, Ryan and Noble (2006) infer that local winds dominate at short periods, and nonlocal (regional) winds dominate for periods longer than 10 days. They estimate the transfer function ("frequency response function" in their terminology) for SSH on the California coast from observed coherences, and find that transfer functions are growing at long time scales of 100 days, although they suggest that this may be due to correlations between forcing mechanisms. Our model results are consistent with these observations. While Ryan and Noble (2006) considered the remote effects of coastal winds, our adjoint sensitivity study also highlights the potential influence of offshore winds on coastal SSH via propagation of inertia–gravity waves, although the spatial scales of the forcing variability may be too large to give this mechanism much importance.

A correlation analysis found that remote coastal winds are highly correlated with SSH, yet they are not the sole driver of SSH variability. The hindcast shows that forcing by local winds is at least as important as remote wind forcing to get the right magnitude of SSH variations. This result emphasizes that correlation does not signify a causal effect, and that is especially true when surface winds tend to have large spatial scales, as they do near the California coast.

e. Limitations

The state estimate provides a useful platform for analyzing the dynamics of the California Current System. With a $\frac{1}{16}°$ grid, it resolves the mesoscale structure and the solution is consistent with observations. It remains, however, the solution to a numerical model and is thus subject to limitations associated with unresolved scales. Though the adjoint method is used to estimate air–sea fluxes, our knowledge of these fluxes and their statistics is still imperfect. The optimization is constrained by NAM winds, which have biases. They also exhibit less temporal variability than observed buoy winds and the spatial structures are overly smooth, especially near the coast. We hypothesize that incorrect forcing at small scales is a major reason that the model may not reproduce the observed tide gauge variability (Fig. 2), even though the model agrees with altimeter SSH offshore. Because the large-scale structure of the modeled ocean is consistent with observations, the adjoint sensitivity analysis is based on realistic topography and stratification, and the mechanisms identified here for propagation of atmospherically forced signals are physical.

It is worth reiterating that the sensitivities to atmospheric forcing quantify the potential effects on SSH, but these effects may never be realized. For instance, the large sensitivities to offshore winds may not have much influence in SSH variability if the winds do not have the spatial and temporal variability needed to produce constructive interference at the target location. The results presented here show that a spatially uniform wind stress perturbation has a reduced effect on coastal SSH, and temporally persistent winds would show a similar result. The adjoint results do identify, however, that inertia–gravity waves are a potentially important mechanism for carrying the effect of offshore winds toward the coast.

The linear sensitivity analysis provides an insight into the physics, though it has obvious limitations, as the true sensitivities are expected to have some degree of nonlinearity. This should not be a substantial source of error for the particular problem examined in this study, because the SSH response to wind perturbations of typical magnitude is mostly linear over the 100-day period analyzed. The larger the perturbation, the sooner we expect the linearity of the response to break down. The linearity of the SSH response in our model results from a combination of the horizontal viscosity of $100\,\mathrm{m}^2\,\mathrm{s}^{-1}$ and the model resolution, weakly unstable flows in the California Current System, and the particular wind perturbations that were considered. There may exist perturbations that would excite a more nonlinear response; we have not probed the entire domain with our forward perturbations. Overall, however, we expect the sensitivities presented here to capture the leading-order effects of atmospheric forcing on coastal SSH.

6. Conclusions

This paper addresses what controls sea surface height variability at one location on the coast. This is a first step in understanding what sustains pressure gradients, and thus determines the geostrophic circulation in the California Current System. To investigate cross-shore pressure gradients one would either use the gradient as a cost function or use the SSH at a point offshore of Port San Luis and take the difference of the sensitivities. The latter separates the two responses for clarity, and, because of linearity, the difference of the sensitivities is the same as the sensitivity of the differences. Addressing alongshore pressure gradients would require examination of SSH sensitivity at several locations along the coast. For both investigations, differencing the responses would shed light on pressure gradient sensitivities and reveal controls on the transport.

The results presented here emphasize the role of stratification in modulating the sensitivity of SSH to air–sea momentum fluxes. Higher stratification in summer increases the sensitivity of coastal SSH to wind stress, relative to lower stratification in winter. In a warming climate, the ocean may become more stratified. Barring other changes in ocean state that would affect the sensitivity of coastal SSH to atmospheric forcing, our analysis suggests that it could imply a higher sensitivity to wind stress and longer-lasting effects of the winds on coastal sea level.

REFERENCES

Alford, M., 2003: Redistribution of energy available for ocean mixing by long-range propagation of internal waves. *Nature,* **21,** 159–163.

Battisti, D., and B. Hickey, 1984: Application of remote wind-forced coastal trapped wave theory to the Oregon and Washington coasts. *J. Phys. Oceanogr.,* **14,** 887–903.

Brink, K., 1991: Coastal-trapped waves and wind-driven currents over the continental-shelf. *Annu. Rev. Fluid Mech.,* **23,** 389–412.

Chapman, D., 1987: Application of wind-forced, long, coastal-trapped wave theory along the California coast. *J. Geophys. Res.,* **92** (C2), 1798–1816.

Checkley, D., and J. Barth, 2009: Patterns and processes in the California current system. *Prog. Oceanogr.,* **83,** 49–64.

Chenillat, F., P. Rivière, X. Capet, P. Franks, and B. Blanke, 2013: California coastal upwelling onset variability: Cross-shore and bottom-up propagation in the planktonic ecosystem. *PLoS ONE,* **8,** e62281, doi:10.1371/journal.pone.0062281.

D'Asaro, E. A., C. C. Eriksen, M. D. Levine, P. Niiler, C. A. Paulson, and P. V. Meurs, 1995: Upper ocean inertial currents forced by a strong storm. Part I: Data and comparisons with linear theory. *J. Phys. Oceanogr.,* **25,** 2909–2936.

de Boyer Montégut, C., G. Madec, A. Fischer, A. Lazar, and D. Iudicone, 2004: Mixed layer depth over the global ocean: An examination of profile data and a profile-based climatology. *J. Geophys. Res.,* **109,** C12003, doi:10.1029/2004JC002378.

Fekete, B. M., C. J. Vorosmarty, and W. Grabs, 2002: High-resolution fields of global runoff combining observed river discharge and simulated water balances. *Global Biogeochem. Cycles,* **16** (3), doi:10.1029/1999GB001254.

Forget, G., 2010: Mapping ocean observations in a dynamical framework: A 2004–06 ocean atlas. *J. Phys. Oceanogr.,* **40,** 1201–1221.

Giering, R., and T. Kaminski, 1998: Recipes for adjoint code construction. *ACM Trans. Math. Software,* **24,** 437–474.

Gill, A., 1982: *Atmosphere–Ocean Dynamics.* Academic Press, 662 pp.

Huyer, A., 1983: Coastal upwelling in the California Current System. *Prog. Oceanogr.,* **12,** 259–284.

Kemp, A. C., B. P. Horton, J. P. Donnelly, M. E. Mann, M. Vermeer, and S. Rahmstorf, 2011: Climate related sea-level variations over the past two millennia. *Proc. Natl. Acad. Sci. USA,* **108,** 11 017–11 022.

Kim, S. Y., 2010: Observations of submesoscale eddies using high-frequency radar-derived kinematic and dynamic quantities. *Cont. Shelf Res.,* **30,** 1639–1655, doi:10.1016/j.csr.2010.06.011.

——, B. D. Cornuelle, and E. J. Terrill, 2009: Anisotropic response of surface currents to the wind in a coastal region. *J. Phys. Oceanogr.,* **39,** 1512–1533.

——, and Coauthors, 2011: Mapping the U.S. West Coast surface circulation: A multiyear analysis of high-frequency radar observations. *J. Geophys. Res.,* **116,** C03011, doi:10.1029/2010JC006669.

Large, W., and S. Pond, 1981: Open ocean momentum flux measurements in moderate to strong winds. *J. Phys. Oceanogr.,* **11,** 324–336.

——, J. C. McWilliams, and S. C. Doney, 1994: Oceanic vertical mixing: A review and a model with a nonlocal boundary layer parameterization. *Rev. Geophys.,* **32,** 363–403.

Losch, M., and P. Heimbach, 2007: Adjoint sensitivity of an ocean general circulation model to bottom topography. *J. Phys. Oceanogr.,* **37,** 377–393.

MacKinnon, J., and M. Gregg, 2005: Near-inertial waves on the New England shelf: The role of evolving stratification, turbulent dissipation, and bottom drag. *J. Phys. Oceanogr.,* **35,** 2408–2424.

MacMynowski, D. G., and E. Tziperman, 2010: Testing and improving ENSO models by process using transfer functions. *Geophys. Res. Lett.,* **37,** L19701, doi:10.1029/2010GL044050.

Marshall, J., A. Adcroft, C. Hill, L. Perelman, and C. Heisey, 1997: A finite-volume, incompressible Navier–Stokes model for studies of the ocean on parallel computers. *J. Geophys. Res.,* **102** (C3), 5753–5766.

Mazloff, M. R., 2012: On the sensitivity of the Drake Passage transport to air–sea momentum flux. *J. Climate,* **25,** 2279–2290.

Moore, A. M., H. G. Arango, E. Di Lorenzo, A. J. Miller, and B. D. Cornuelle, 2009: An adjoint sensitivity analysis of the southern California Current circulation and ecosystem. *J. Phys. Oceanogr.,* **39,** 702–720.

Nicholls, R. J., and A. Cazenave, 2010: Sea-level rise and its impact on coastal zones. *Science,* **328,** 1517–1520.

Powell, B., H. Arango, A. Moore, E. D. Lorenzo, R. Milliff, and D. Foley, 2008: 4DVAR data assimilation in the Intra-Americas Sea with the Regional Ocean Modeling System (ROMS). *Ocean Modell.,* **23,** 130–145.

Pringle, J. M., and K. Riser, 2003: Remotely forced nearshore upwelling in Southern California. *J. Geophys. Res.,* **108,** 3131, doi:10.1029/2002JC001447.

—— and E. Dever, 2009: Dynamics of wind-driven upwelling and relaxation between Monterey Bay and Point Arena: Local-, regional-, and gyre-scale controls. *J. Geophys. Res.,* **114,** C07003, doi:10.1029/2008JC005016.

Ryan, H. F., and M. A. Noble, 2006: Alongshore wind forcing of coastal sea level as a function of frequency. *J. Phys. Oceanogr.,* **36,** 2173–2184.

Rykaczewski, R., and D. Checkley, 2008: Influence of ocean winds on the pelagic ecosystem in upwelling regions. *Proc. Natl. Acad. Sci. USA,* **105,** 1965–1970.

Sasaki, H., and P. Klein, 2012: SSH wavenumber spectra in the North Pacific from a high-resolution realistic simulation. *J. Phys. Oceanogr.,* **42,** 1233–1241.

Shearman, R., 2005: Observations of near-inertial current variability on the New England shelf. *J. Geophys. Res.,* **110,** C02012, doi:10.1029/2004JC002341.

Sobarzo, M., R. Shearman, and S. Lentz, 2007: Near-inertial motions over the continental shelf off Concepción, central Chile. *Prog. Oceanogr.,* **75,** 348–362.

Stammer, D., and Coauthors, 2003: Volume, heat, and freshwater transports of the global ocean circulation 1993–2000, estimated from a general circulation model constrained by World Ocean Circulation Experiment (WOCE) data. *J. Geophys. Res.,* **108,** 3007, doi:10.1029/2001JC001115.

Todd, R., D. Rudnick, M. Mazloff, R. Davis, and B. Cornuelle, 2011: Poleward flows in the southern California Current System: Glider observations and numerical simulation. *J. Geophys. Res.,* **116,** C02026, doi:10.1029/2010JC006536.

——, ——, ——, B. Cornuelle, and R. Davis, 2012: Thermohaline structure in the California Current System: Observations and modeling of spice variance. *J. Geophys. Res.,* **117,** C02008, doi:10.1029/2011JC007589.

Tulloch, R., C. Hill, and O. Jahn, 2011: Possible spreadings of buoyant plumes and local coastline sensitivities using flow syntheses from 1992 to 2007. *Monitoring and Modeling the Deepwater Horizon Oil Spill: A Record-Breaking Enterprise, Geophys. Monogr.,* Vol. 195, Amer. Geophys. Union, 245–255.

Veneziani, M., C. A. Edwards, and A. M. Moore, 2009: A central California coastal ocean modeling study: 2. Adjoint sensitivities to local and remote forcing mechanisms. *J. Geophys. Res.,* **114,** C04020, doi:10.1029/2008JC004775.

Wunsch, C., 2006: *Discrete Inverse and State Estimation Problems: With Geophysical Fluid Applications.* Cambridge University Press, 384 pp.

——, and P. Heimbach, 2007: Practical global oceanic state estimation. *Physica D,* **230,** 197–208.

Zhang, X., B. Cornuelle, and D. Roemmich, 2011: Adjoint sensitivity of the Niño-3 surface temperature to wind forcing. *J. Climate,* **24,** 4480–4493.

——, ——, and ——, 2012: Sensitivity of western boundary transport at the mean north equatorial current bifurcation latitude to wind forcing. *J. Phys. Oceanogr.,* **42,** 2056–2072.